SANDIA REPORT
SAND2020-9716
Printed September 2020

Sandia National Laboratories

An Adaptive and Scalable Meshfree Framework for Extreme Deformation and Failure in Solids

Alejandro Mota, Julia A. Plews, Brandon Talamini, Avery Rock

Prepared by
Sandia National Laboratories
Albuquerque, New Mexico 87185
Livermore, California 94550

Issued by Sandia National Laboratories, operated for the United States Department of Energy by National Technology & Engineering Solutions of Sandia, LLC.

Available to DOE and DOE contractors from

U.S. Department of Energy
Office of Scientific and Technical Information
P.O. Box 62
Oak Ridge, TN 37831

Telephone: (865) 576-8401
Facsimile: (865) 576-5728
E-Mail: reports@osti.gov
Online ordering: http://www.osti.gov/scitech

Available to the public from

U.S. Department of Commerce
National Technical Information Service
5301 Shawnee Road
Alexandria, VA 22312

Telephone: (800) 553-6847
Facsimile: (703) 605-6900
E-Mail: orders@ntis.gov
Online order: https://classic.ntis.gov/help/order-methods

ABSTRACT

Recent developments at Sandia in meshfree methods have delivered improved robustness in solid mechanics problems that prove difficult for traditional Lagrangian, mesh-based finite elements. Nevertheless, there remains a limitation in accurately predicting *very large* material deformations. It seems robust meshfree discretizations and integration schemes are necessary, but not sufficient, to close this capability gap. This state of affairs directly impacts current and future LEPs, whose simulation needs are not well met for extremely large deformation problems.

We propose to use a new numerical framework, the *Optimal Transportation Meshfree* (OTM) method enhanced by *meshfree adaptivity*, as we believe that a combination of both will provide a novel way to close this capability gap.

ACKNOWLEDGMENT

We thank Jay Foulk, Jake Koester, Mike Tupek and Prof. Bo Li of Case Western Reserve University for valuable discussions and suggestions.

CONTENTS

LIST OF FIGURES

This page intentionally left blank.

1. INTRODUCTION

Recent developments at Sandia in meshfree methods have delivered improved robustness in solid mechanics problems that prove difficult for traditional Lagrangian, mesh-based finite elements. Nevertheless, there remains a limitation in accurately predicting *very large* material deformations. It seems robust meshfree discretizations and integration schemes are necessary, but not sufficient, to close this capability gap. This state of affairs directly impacts current and future LEPs, whose simulation needs are not well met for extremely large deformation problems. Applications include:

- ballistic impact spanning the ordnance regime ($\sim 100 - 3000$ m/s impact velocities)
- impact into soft targets
- ductile failure
- shear-banding and localization in metals and bonded granular materials
- localized melting and other phase transitions

We seek to answer the technical question: can we build on the recent advances at Sandia in meshless simulation, and develop an accurate and robust computational approach for predicting material response under extreme deformation? Our hypothesis is that *meshfree adaptivity* is one of the keys to resolving this problem.

State-of-the-art methods for tackling extreme deformations have critical deficiencies:

- Eulerian hydrocodes: specialized for fluid-like behavior in problems like hypervelocity impact, not the deformations of solids. Induce numerical smearing of material states, problematic for modeling plastic deformation. Also lack a well-defined surface representation, crucial for modeling contact.
- Lagrangian mesh-based finite element methods: existing methods to address mesh distortion are ad hoc, are not sufficiently robust or accurate.
- Lagrangian meshfree methods: No adaptivity resources in the implementations currently available at Sandia, and a search of the open literature yields very little work in this direction. Robust contact algorithms for these discretization schemes have likewise not received much attention. In some versions of Lagrangian meshfree, this is compounded by difficulties in identifying and representing the surface without a mesh.

Recent work at Sandia has improved the numerical stability and geometry-to-simulation turnaround time for meshfree methods. We aim to retain these advances to the greatest extent possible, while tackling the challenges noted above. We propose to use a new numerical framework, the *Optimal Transportation Meshfree* (OTM) method, as we believe it has properties beneficial to close this capability gap:

- It is a *rigorous mathematical framework* based on variational minimization principles. The discretization procedure is thus amenable to well-established accuracy and stability analyses, which provides tools for error estimation, and a means to detect incipient instabilities. Furthermore, the variational principle approach provides a meaningful objective function for *goal oriented adaptivity.*
- The basis functions are interpolating, at least on convex boundaries, which in practical terms means that the *surface is directly represented by the nodal points*.

The Optimal Transportation Meshfree (OTM) method is a meshfree updated Lagrangian methodology, which combines concepts from Optimal Transportation theory with material-point sampling and local maximum entropy (LME) meshfree approximation, and overcomes the essential difficulties in grid- based Lagrangian and Eulerian finite element methods. In OTM, the inertial action in space and time is discretized within a strictly variational framework [17, 21, 22, 19, 18, 20]. The resulting discretization is the result of restricting the inertial action to mass measures concentrated on material points undergoing piecewise-rectilinear motions. The density of such mass measures and the constrained minimization structure of the problem confers the discretization robust convergence properties. The framework also results in proper mass matrices and inertia forces in the presence of continuously varying spatial interpolation, geometrically exact mass transport and satisfaction of the continuity equation. Finally, fields requiring differentiation, such as deformation and velocity fields, are interpolated from nodal values using LME shape functions, and possess a Kronecker-delta property at the boundary, which enables the direct imposition of displacement boundary conditions, unlike other meshfree methods.

In this work, we propose to advance this framework in several key areas to meet the needs of the laboratories:

- implement the theory of optimal transportation, including the ability to choose between different approximation bases;
- take advantage of the meshfree framework to develop adaptivity strategies, to resolve local geometric features and material instabilities;
- exploit the variational structure of the method to incorporate material models to predict shear banding, fracture, and phase transitions in solids.

2. FORMULATION OF THE FINITE DEFORMATION SOLID DYNAMICS PROBLEM

We start by defining the standard finite deformation variational formulation to establish notation before presenting the formulation of the meshless method.

2.1. Variational formulation

Let $I := \{t \in [t_0, t_N]\}$ be a closed time interval with $t_0 < t_N$, and $t_0, t_N \in \mathbb{R}$. Then consider a body as the regular open set $\Omega \subset \mathbb{R}^3$ undergoing a motion described by the mapping $\boldsymbol{x} = \boldsymbol{\varphi}(\boldsymbol{X}, t) : \Omega \times I \to \mathbb{R}^3$, where $\boldsymbol{X} \in \Omega$ and $t \in I$. Assume that the boundary of the body is $\partial\Omega = \partial_{\boldsymbol{\varphi}}\Omega \cup \partial_{\boldsymbol{T}}\Omega$ with unit normal $\boldsymbol{N}$, where $\partial_{\boldsymbol{\varphi}}\Omega$ is a prescribed position boundary, $\partial_{\boldsymbol{T}}\Omega$ is a prescribed traction traction boundary, and $\partial_{\boldsymbol{\varphi}}\Omega \cap \partial_{\boldsymbol{T}}\Omega = \emptyset$. The prescribed boundary positions or Dirichlet boundary conditions are $\boldsymbol{\chi} : \partial_{\boldsymbol{\varphi}}\Omega \times I \to \mathbb{R}^3$. The prescribed boundary tractions or Neumann boundary conditions are $\boldsymbol{T} : \partial_{\boldsymbol{T}}\Omega \times I \to \mathbb{R}^3$. Let $\boldsymbol{F} := \operatorname{Grad} \boldsymbol{\varphi}$ be the deformation gradient. Let the initial position and velocity at time t_0 be $\boldsymbol{x}_0 \equiv \boldsymbol{X} : \Omega \to \mathbb{R}^3$, and $\boldsymbol{v}_0 : \Omega \to \mathbb{R}^3$, correspondingly. Let also $\rho_0 \boldsymbol{B} : \Omega \to \mathbb{R}^3$ be the body force, with ρ_0 the mass density in the reference configuration. Furthermore, introduce the kinetic energy of the body as

$$T(\dot{\boldsymbol{\varphi}}) := \frac{1}{2} \int_\Omega \rho_0 \dot{\boldsymbol{\varphi}} \cdot \dot{\boldsymbol{\varphi}} \, \mathrm{d}V, \tag{2.1}$$

and its potential energy as

$$V(\boldsymbol{\varphi}) := \int_\Omega A(\boldsymbol{F}, \boldsymbol{Z}) \, \mathrm{d}V - \int_\Omega \rho_0 \boldsymbol{B} \cdot \boldsymbol{\varphi} \, \mathrm{d}V - \int_{\partial_{\boldsymbol{T}}\Omega} \boldsymbol{T} \cdot \boldsymbol{\varphi} \, \mathrm{d}S, \tag{2.2}$$

in which $A(\boldsymbol{F}, \boldsymbol{Z})$ is the Helmholtz free-energy density and $\boldsymbol{Z}$ is a collection of internal variables. The Lagrangian function of the body is then

$$L(\boldsymbol{\varphi}, \dot{\boldsymbol{\varphi}}) := T(\dot{\boldsymbol{\varphi}}) - V(\boldsymbol{\varphi}), \tag{2.3}$$

which gives rise to the action functional

$$S[\boldsymbol{\varphi}] := \int_I L(\boldsymbol{\varphi}, \dot{\boldsymbol{\varphi}}) \, \mathrm{d}t. \tag{2.4}$$

According to the Variational Principle of Hamilton, the equation of motion is obtained by finding the critical point of the action functional $S[\boldsymbol{\varphi}]$ over the Sobolev space $W_2^1(\Omega \times I)$ that is comprised of all functions that are square-integrable and have square-integrable first derivatives [24]. Define

$$\mathcal{S} := \left\{ \boldsymbol{\varphi} \in W_2^1(\Omega \times I) : \boldsymbol{\varphi} = \boldsymbol{\chi} \text{ on } \partial_{\boldsymbol{\varphi}}\Omega \times I; \boldsymbol{\varphi} = \boldsymbol{x}_0 \text{ on } \Omega \times t_0 \right\} \tag{2.5}$$

and

$$\mathcal{V} := \left\{ \boldsymbol{\xi} \in W_2^1(\Omega \times I) : \boldsymbol{\xi} = \mathbf{0} \text{ on } \partial_{\boldsymbol{\varphi}}\Omega \times I \cup \Omega \times t_0 \right\} \tag{2.6}$$

where $\boldsymbol{\xi}$ is a test function. This leads to

$$\begin{aligned} \delta S := DS[\boldsymbol{\varphi}](\boldsymbol{\xi}) &= \int_I \left(\frac{\partial L}{\partial \boldsymbol{\varphi}} \cdot \boldsymbol{\xi} + \frac{\partial L}{\partial \dot{\boldsymbol{\varphi}}} \cdot \dot{\boldsymbol{\xi}} \right) \, \mathrm{d}t = \int_I \left(\frac{\partial L}{\partial \boldsymbol{\varphi}} - \frac{\mathrm{d}}{\mathrm{d}t} \frac{\partial L}{\partial \dot{\boldsymbol{\varphi}}} \right) \cdot \boldsymbol{\xi} \, \mathrm{d}t \\ &= \int_I \left[\int_\Omega \left(\rho_0 \boldsymbol{B} \cdot \boldsymbol{\xi} - \boldsymbol{P} : \operatorname{Grad} \boldsymbol{\xi} \right) \, \mathrm{d}V + \int_\Omega \rho_0 \dot{\boldsymbol{\varphi}} \cdot \dot{\boldsymbol{\xi}} \, \mathrm{d}V + \int_{\partial_{\boldsymbol{T}}\Omega} \boldsymbol{T} \cdot \boldsymbol{\xi} \, \mathrm{d}S \right] \, \mathrm{d}t \\ &= \int_I \left[\int_\Omega \left(\operatorname{Div} \boldsymbol{P} + \rho_0 \boldsymbol{B} - \rho_0 \ddot{\boldsymbol{\varphi}} \right) \cdot \boldsymbol{\xi} \, \mathrm{d}V + \int_{\partial_{\boldsymbol{T}}\Omega} \boldsymbol{T} \cdot \boldsymbol{\xi} \, \mathrm{d}S \right] \, \mathrm{d}t = 0, \end{aligned} \tag{2.7}$$

where $\boldsymbol{P} = \partial A / \partial \boldsymbol{F}$ denotes the first Piola-Kirchhoff stress. The Euler-Lagrange equation corresponding to (2.4) is then

$$\operatorname{Div} \boldsymbol{P} + \rho_0 \boldsymbol{B} = \rho_0 \ddot{\boldsymbol{\varphi}} \quad \text{in} \quad \Omega \times I, \tag{2.8}$$

with the initial conditions

$$\begin{aligned} \boldsymbol{\varphi}(\boldsymbol{X}, t_0) &= \boldsymbol{x}_0 \quad \text{in} \quad \Omega, \\ \dot{\boldsymbol{\varphi}}(\boldsymbol{X}, t_0) &= \boldsymbol{v}_0 \quad \text{in} \quad \Omega. \end{aligned} \tag{2.9}$$

and the boundary conditions

$$\begin{aligned} \boldsymbol{\varphi}(\boldsymbol{X}, t) &= \boldsymbol{\chi} \quad \text{on} \quad \partial_{\boldsymbol{\varphi}}\Omega \times I, \\ \boldsymbol{P}\boldsymbol{N} &= \boldsymbol{T} \quad \text{on} \quad \partial_{\boldsymbol{T}}\Omega \times I. \end{aligned} \tag{2.10}$$

2.2. Spatial Discretization by Local Maximum Entropy (LME) Shape Functions

The domain under consideration is discretized by two sets of points, called nodes and material points or points for short. The nodes play the same role as in the standard finite element method, and the points play a similar role as the integration points [17]. Each node has a set of points associated to it called the influence domain. Conversely, each point has a set of nodes associated to it called the support domain. The influence and support domains are the data structures that maintain the connectivity between the nodes and points. They change dynamically as the simulation advances. See Figure 2-1.

Next we introduce the spatial discretization for the field $\boldsymbol{\varphi}$ and its test function $\boldsymbol{\xi}$ as

$$\begin{aligned} \boldsymbol{\varphi}_h(\boldsymbol{X}) &:= N_a(\boldsymbol{X}) \boldsymbol{x}_a \in \mathcal{S}_h, \\ \boldsymbol{\xi}_h(\boldsymbol{X}) &:= N_a(\boldsymbol{X}) \boldsymbol{\xi}_a \in \mathcal{V}_h, \end{aligned} \tag{2.11}$$

in which $\mathcal{S}_h \subset \mathcal{S}$ and $\mathcal{V}_h \subset \mathcal{V}$ are finite-dimensional subspaces of $\mathcal{S}$ and $\mathcal{V}$, respectively. The local maximum entropy shape functions are defined as

$$\begin{aligned} Z_a(\boldsymbol{X}_p, \boldsymbol{\lambda}) &:= \exp\left[-\beta||\boldsymbol{X}_p - \boldsymbol{X}_a|| + \boldsymbol{\lambda}\cdot(\boldsymbol{X}_p - \boldsymbol{X}_a)\right], \\ Z(\boldsymbol{X}_p, \boldsymbol{\lambda}) &:= \sum_{a=1}^{N_p} Z_a(\boldsymbol{X}_p, \boldsymbol{\lambda}), \\ \boldsymbol{\lambda}_p &:= \arg\min_{\boldsymbol{\lambda}} Z(\boldsymbol{X}_p, \boldsymbol{\lambda}), \\ N_a(\boldsymbol{X}_p) &:= \frac{Z_a(\boldsymbol{X}_p, \boldsymbol{\lambda}_p)}{Z(\boldsymbol{X}_p, \boldsymbol{\lambda}_p)}, \end{aligned} \tag{2.12}$$

where β is a locality parameter that narrows or spreads the support of the shape functions, $\boldsymbol{\lambda}$ is a Lagrange multiplier that enforces the first order consistency condition, and N_p is the number of support nodes for a specific point p. The normalization is effected so that the shape functions satisfy the partition of unity condition.

The minimization to find the Lagrange multiplier $\boldsymbol{\lambda}_p$ is carried out numerically, typically by means of a Newton-type scheme. We will explore in Chapter 5 how well-conditioned this minimization is, in particular in the presence of adaptivity, where nodes and points are inserted or removed from the domain. For a more thorough discussion of the local maximum entropy shape functions, the reader is referred to Arroyo and Ortiz [2], Li [17], Li et al. [21], and Weissenfels and Wriggers [33], and references therein.

2.3. Temporal Discretization by a Two-Step Integration Algorithm

Here, we follow the time integration scheme proposed by Li [17] and Li et al. [21], which does not assume a constant time step as in Weissenfels and Wriggers [33]. The OTM method is an updated Lagrangian scheme. Assume that the time interval $I := \{t \in [t_0, t_N]\}$ is discretized by a sequence of time values $t_0, \ldots, t_k, \ldots, t_N$, and that the configuration of the body is known at time t_k. The task is to update the configuration such that $\Omega_{k+1} := \varphi_k(\Omega_k, t_k)$, as shown in Figure 2-2. Define the diagonal lumped mass matrix as $\boldsymbol{M}_k$, where each entry $m_a^{(k)}$ is computed as

$$m_a^{(k)} := \sum_{p=1}^{N_a} N_a(\boldsymbol{X}_p)\rho_p^{(k)} V_p^{(k)}, \tag{2.13}$$

where $\rho_p^{(k)}$ is the mass density and $V_p^{(k)}$ is the volume associated with point p, correspondingly; and N_a is the number of points in the influence domain of node a. For convenience, the positions, densities and volumes of the points in the discretization are initialized by means of a standard tetrahedral mesh. Then, the nodal linear momentum $\boldsymbol{l}_k$ may be computed as

$$\begin{aligned} \boldsymbol{l}_k &:= \boldsymbol{M}_k \boldsymbol{v}_k, \\ \boldsymbol{v}_{k+1} &:= \frac{\boldsymbol{X}_{k+1} - \boldsymbol{X}_k}{t_{k+1} - t_k}. \end{aligned} \tag{2.14}$$

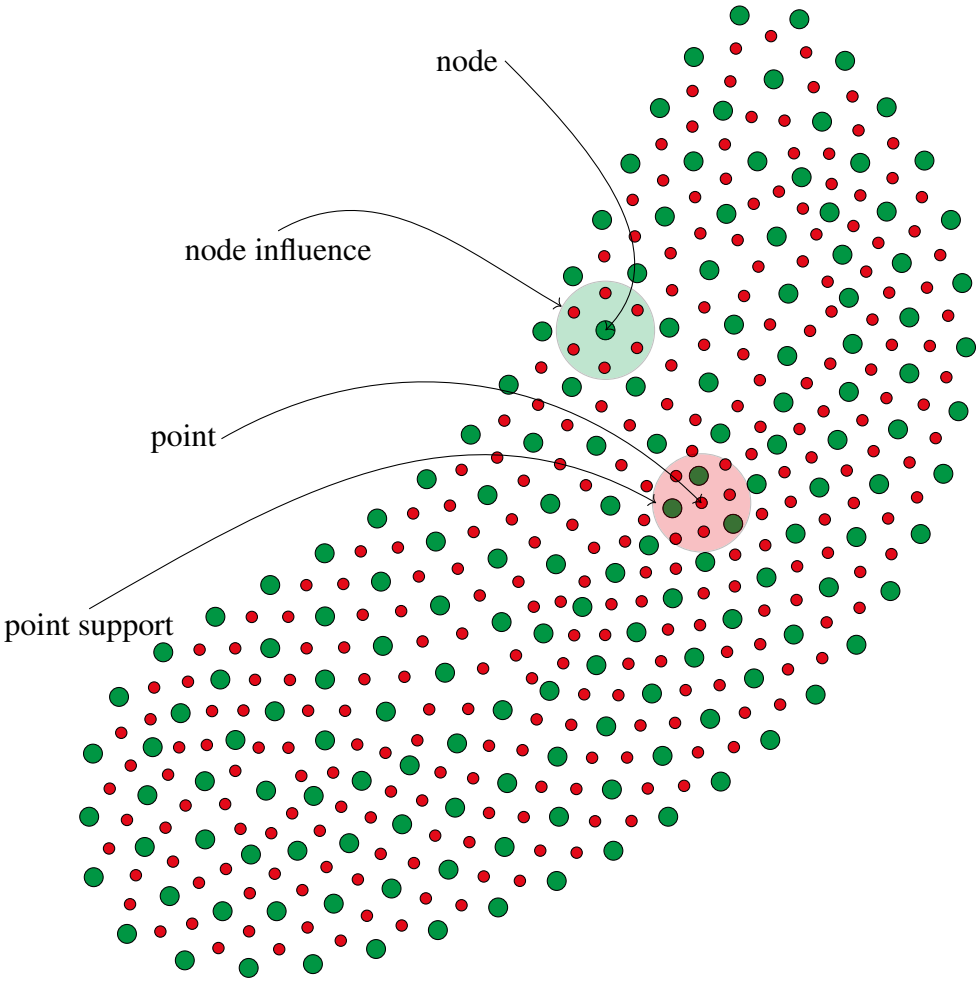

Figure 2-1. A domain discretized by nodes (green) and points (red) for use by the OTM method. Also shown are nodes in the support domain (light red) of a point, and points in the influence domain (light green) of a node. The support and influence are recomputed every certain number of time steps that is chosen beforehand.

Note that this definition of the linear momentum is different than the one used in Li [17] and Li et al. [21], where it is computed by means of the point masses and LME functions. This expression, however, is more efficient computationally and does not seem to introduce adverse effects in our calculations and those of Li [23]. The procedure that effects the integration in time is shown in Algorithm 1.

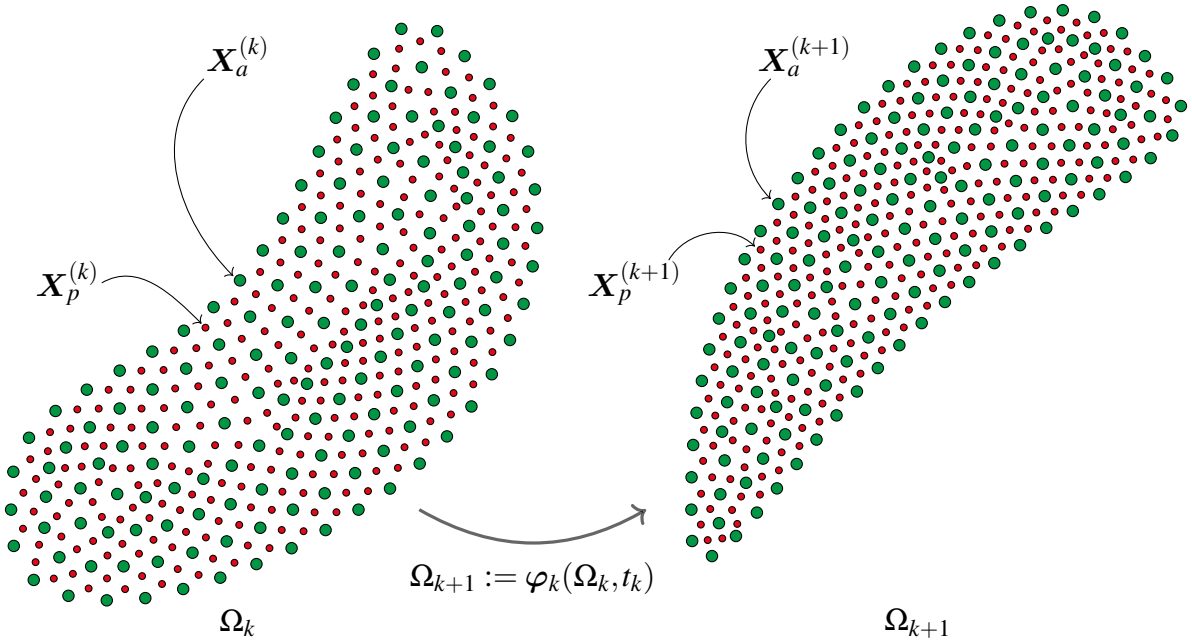

Figure 2-2. Two subdomains Ω_k and Ω_{k+1}. The task of the OTM method is to update the configuration such that $\Omega_{k+1} := \varphi_k(\Omega_k, t_k)$

Initialize nodal positions $\boldsymbol{X}_a^{(-1)}$ and $\boldsymbol{X}_a^{(0)}$, and times t_{-1} and t_0
Initialize point positions $\boldsymbol{X}_p^{(0)}$, volumes $V_p^{(0)}$, densities $\rho_p^{(0)}$, and masses m_p
Initialize total deformation gradient $\boldsymbol{F}_p^{(0)}$
$k \leftarrow 0$
repeat ▷ time integration loop
    Compute support and influence domains in Figure 2-1 ▷ Optional adaptivity here
    Compute $N_a(\boldsymbol{X}_p^{(k)})$ and $\mathrm{Grad} N_a(\boldsymbol{X}_p^{(k)})$ by (2.12)
    Compute $\boldsymbol{M}_k$ by (2.13) and $\boldsymbol{l}_k$ by (2.14)
    Compute residual force $\boldsymbol{f}_k$ ▷ Assemble in finite element fashion
    Update time step ▷ We use a conservative Courant condition estimate
    $\boldsymbol{X}_a^{(k+1)} \leftarrow \boldsymbol{X}_a^k + (t_{k+1} - t_k)\boldsymbol{M}_k^{-1}\left(\boldsymbol{l}_k + \frac{t_{k+1}-t_{k-1}}{2}\boldsymbol{f}_k\right)$
    $\boldsymbol{X}_p^{(k+1)} \leftarrow \sum_{a=1}^{N_p} N_a(\boldsymbol{X}_p^{(k)})\boldsymbol{X}_a^{(k+1)}$
    $\triangle \boldsymbol{F}_p^{(k+1)} \leftarrow \sum_{a=1}^{N_p} \mathrm{Grad} N_a(\boldsymbol{X}_p^{(k)})\boldsymbol{X}_a^{(k+1)}$
    $\boldsymbol{F}_p^{(k+1)} \leftarrow \triangle \boldsymbol{F}_p^{(k+1)} \boldsymbol{F}_p^k$
    $V_p^{(k+1)} \leftarrow \det \triangle \boldsymbol{F}_p^{(k+1)} V_p^k$
    $\rho_p^{(k+1)} \leftarrow \frac{m_p}{V_p^{(k+1)}}$
    $k \leftarrow k+1$
until $k = N$ ▷ N is the total number of time steps

Algorithm 1 Optimal Transportation Meshfree method for solid transient dynamics.

3. IMPLEMENTATION

The OTM method was implemented in the Lagrangian Grid Reconnection (LGR) performance-portable toolkit written by Sandia National Laboratories [15].[1] LGR is fundamentally designed from the ground up for adaptivity, a key component of our purposes. It has minimal dependencies, enabling rapid prototyping of ideas and quick build-test turnaround times. The performance portability of LGR is based on raw CUDA code, the Thrust library, and C++14 standard constructs. This does not prevent LGR to be interoperable with other CUDA-enabled libraries, such as Kokkos or ArborX. LGR's data access patterns are designed for fast access and minimal data race conditions on NVidia GPU threaded architectures. With the help of the LGR framework, we were able to gain valuable experience developing portable algorithms and testing complex code for correctness and performance on both the CPU and GPU without any algorithm duplication. Furthermore, we find that the OTM method as described in Algorithm 1 is amenable to performance on GPU architectures, although further exploration and optimization are required. We observed that our OTM implementation achieved an utilization of the GPU above 90%.

3.1. Geometric Search

The computation of the support and influence domains defined in Figure 2-1 requires geometric searches that are performant both in the CPU and GPU. To this end, we utilize ArborX,[2] an open-source library designed to provide performance portable algorithms for geometric search. ArborX is based on Kokkos[3] and Thrust[4] libraries to deliver performance on both CPU and GPU architectures. Using these libraries, we developed a reusable, performance-portable search library interface for LGR and used it to build the necessary support and influence domains for our OTM implementation.

An example of the gains obtained by performance portability is shown in Figure 3-1, where we plot a comparison of CPU and GPU wall time execution for the Taylor bar simulation of Chapter 4 with different numbers of points.

[1] LGR is available on GitHub: `https://github.com/SNLComputation/LGR`.
[2] ArborX is available on GitHub: `https://github.com/arborx/ArborX` .
[3] Kokkos is available on GitHub: `https://github.com/kokkos/kokkos`.
[4] Thrust is available on GitHub: `https://github.com/thrust/thrust`.

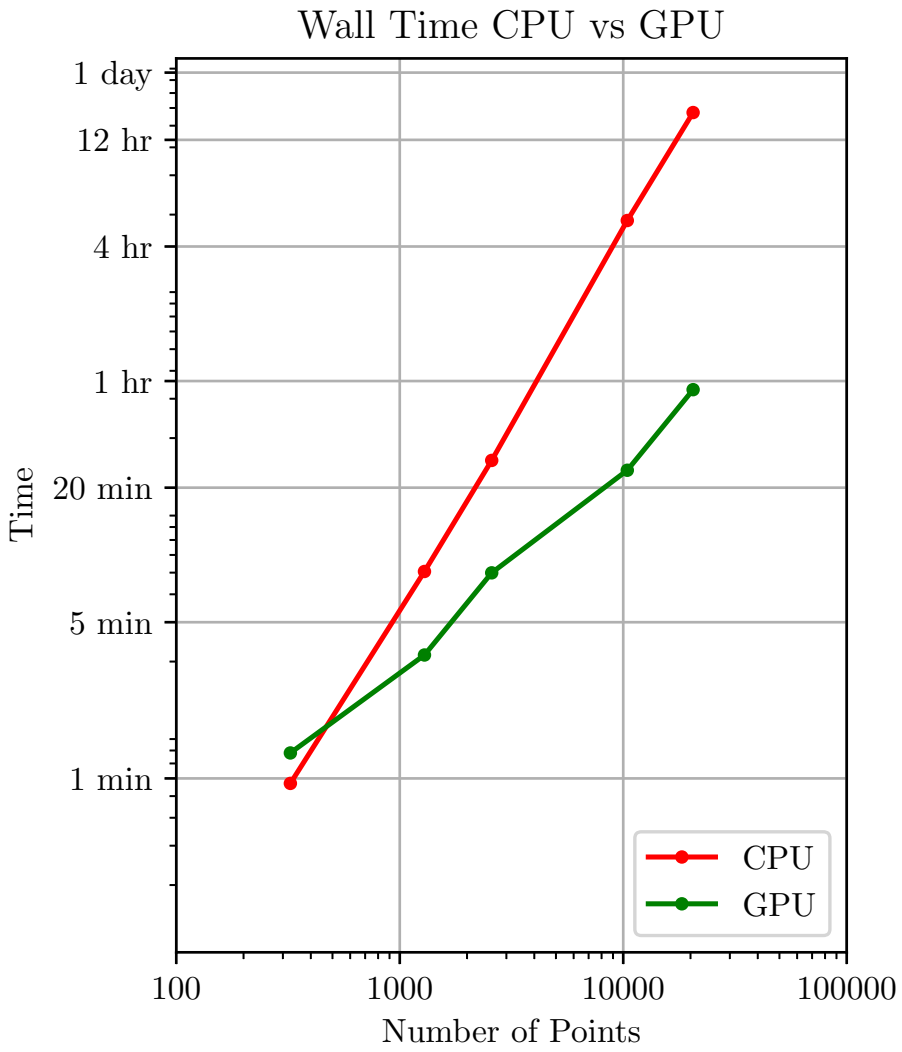

Figure 3-1. Comparison of CPU and GPU wall time execution for the Taylor bar simulation of Chapter 4 with different numbers of points.

4. VERIFICATION BY TAYLOR ANVIL TEST

The impact of a Taylor bar is a common use case to induce extremely large deformation in metals [31, 34, 35]. This is a prime example for the use of numerical simulation methods capable of representing extreme large deformation. The geometry of the cylinder and impact speed is shown in Figure 4-1

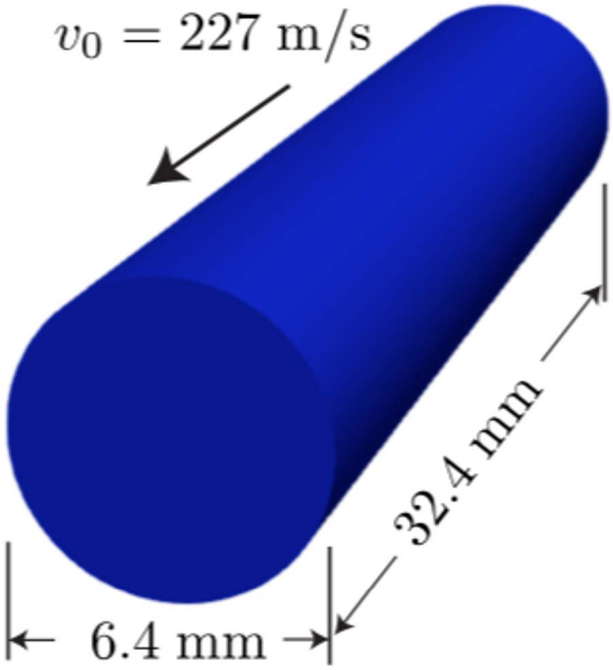

Figure 4-1. Geometry and initial velocity of the copper Taylor bar subjected to impact on a rigid surface.

4.1. Results from Our OTM Implementation

The cylinder is assumed to be made of copper, with a density of 8930kg/m^3. The Young's modulus and Poisson's ratio are 117 GPa and 0.35, respectively. We employ a rate-independent J2 plasticity constitutive model with power law hardening [28]. The yield strength and hardening modulus are 400 MPa and 100 MPa, respectively. The cylinder is initially in contact with the rigid surface.We use two different contact algorithms, one based on enforcing the displacement perpendicular to the rigid surface to be zero, and another based on a penalty coefficient. Both algorithms produce results with very minor differences. We run the simulation from 0μs to 100μs, and we show the resulting deformed configurations in Figure 4-2.

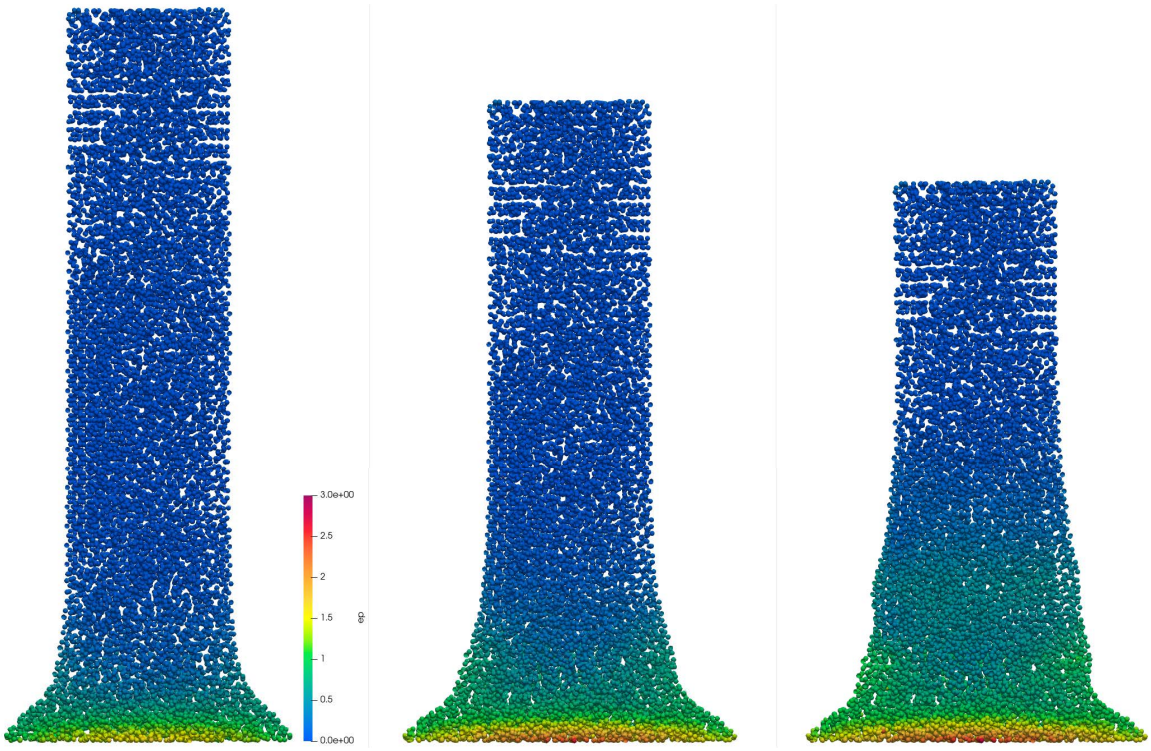

Figure 4-2. Deformed configuration of the Taylor bar obtained with our OTM implementation at 20μs, 40μs, and 80μs. The color contour shows the equivalent plastic strain ε^{p}.

4.2. Comparison to Other Works

It is difficult to validate against other numerical computation results, mainly because published results tend to show deformed configurations and color scales for a field as we show here, without making reference to a precise metric. Nevertheless, we include some results obtained by other authors for reference.

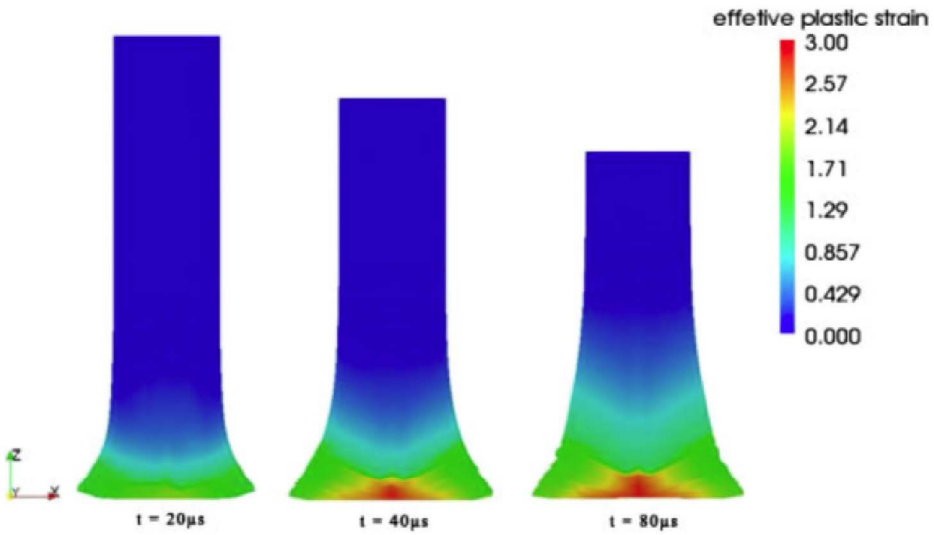

Figure 14. Taylor-anvil impact test of copper specimen at 227 m/s impact velocity. Distributions of effective plastic strain at 20, 40 and 80 μs.

Figure 4-3. Deformed configuration of the Taylor bar at 20μs, 40μs, and 80μs. The color contour shows the equivalent plastic strain ε^p. Taken from Li et al. [21].

A comparison between our results in Figure 4-2 and those of Figures 4-3 to 4-5 leads us to conclude that the behavior that we obtain with our OTM implementation is qualitatively correct. More verification and validations studies are needed, but those are in the scope of future work.

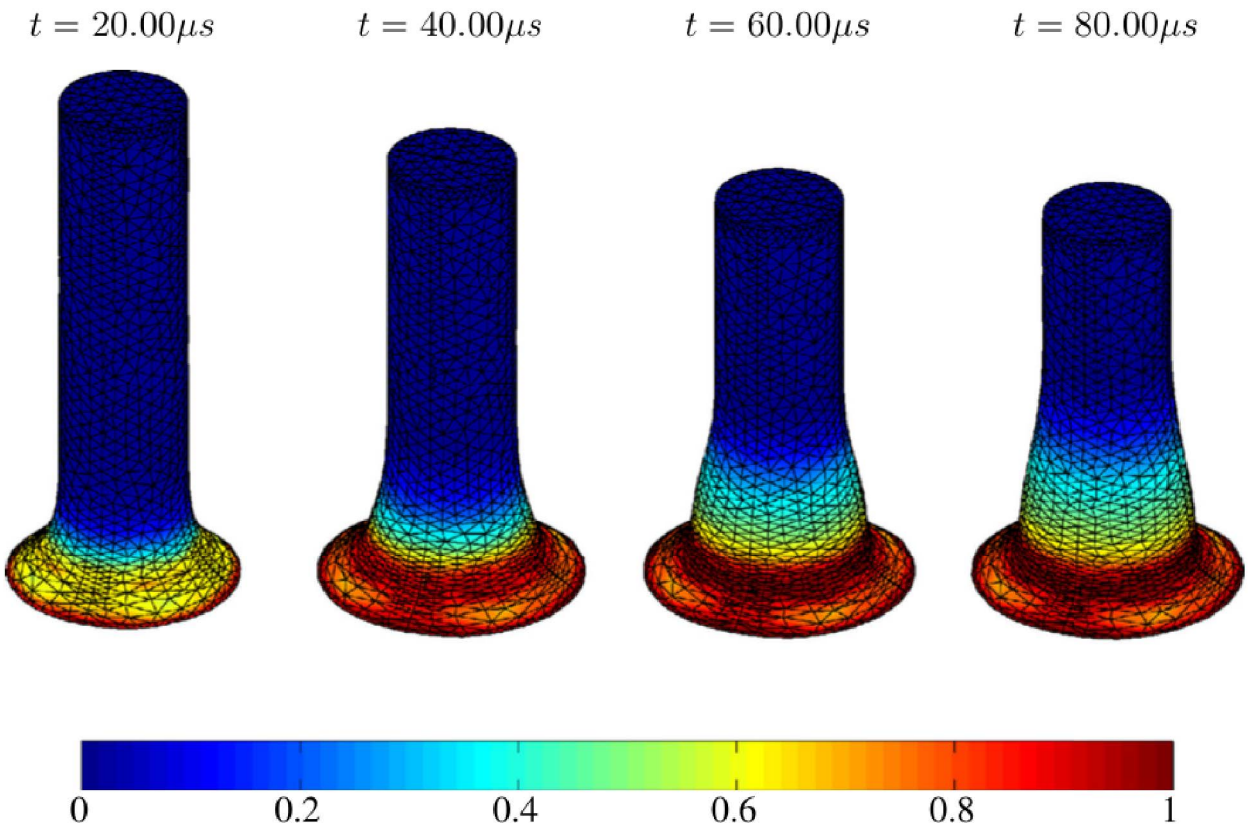

Figure 4-4. Deformed configuration of the Taylor bar at 20μs, 40μs, 60μs, and 80μs. The color contour shows the equivalent plastic strain ε^p. Taken from Aguirre et al. [1].

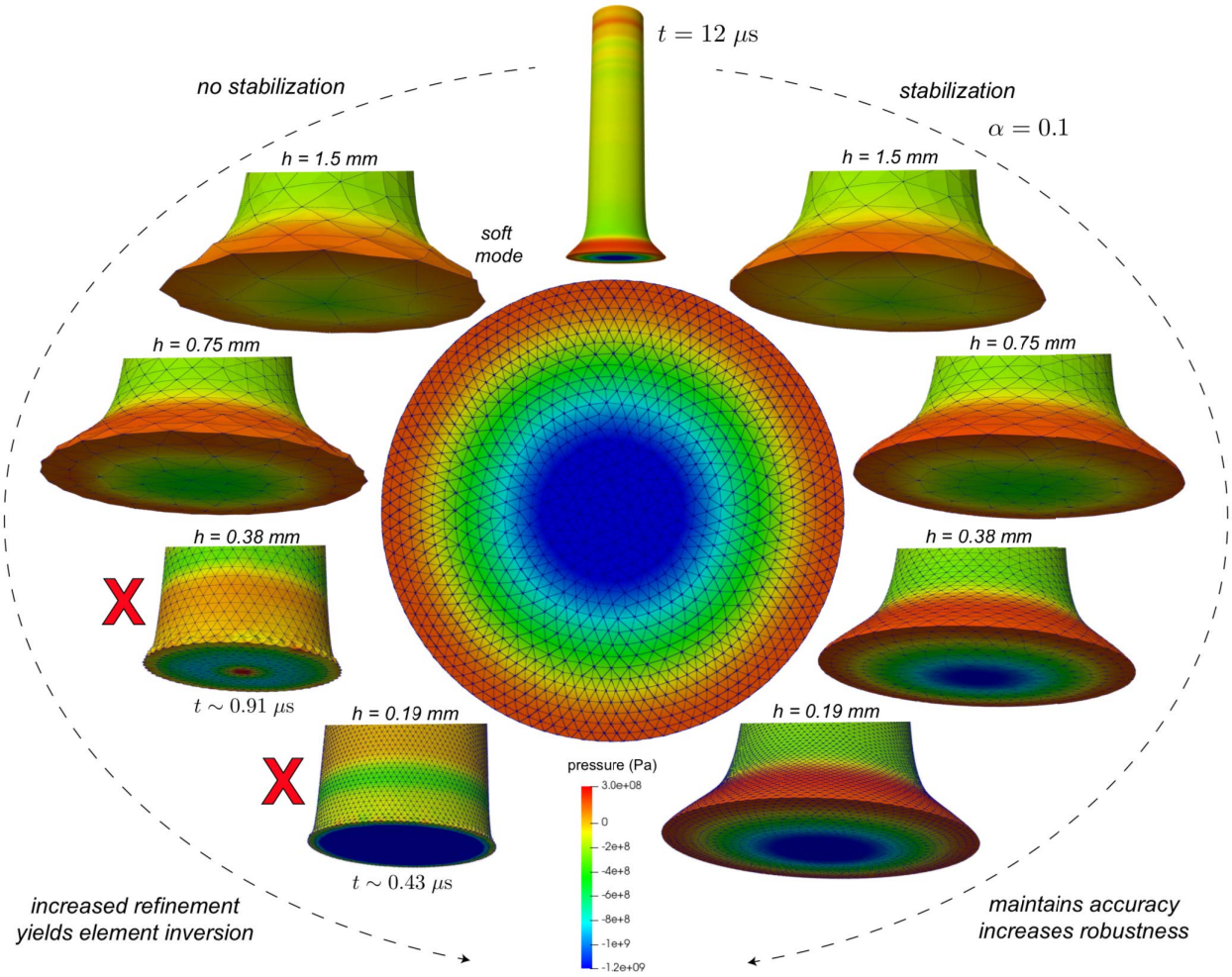

Figure 4-5. Deformed configuration of the Taylor bar at 12μs. The color contour shows the pressure p. Taken from Foulk et al. [11].

5. ADAPTIVITY IN THE OTM METHOD

One of the key aspects of our LDRD project is to determine the effects of meshfree adaptivity in enabling these kinds of methods to access regimes of extreme deformation. Although there is no mesh associated with meshless methods, and thus no possibility of extreme mesh distortion or entanglement, there are regimes where the extreme deformation may lead to an undesirable distributions of nodes and points. As en example, we run the Taylor bar case from Chapter 4, increasing the impact velocity from 227m/s to 750m/s, and at 37μs we obtain the configuration shown in Figure 5-1. Note the spread of the points as the cylinder flattens against the rigid surface. This is undesirable for fine resolution of the fields, and thus the need for adaptivity.

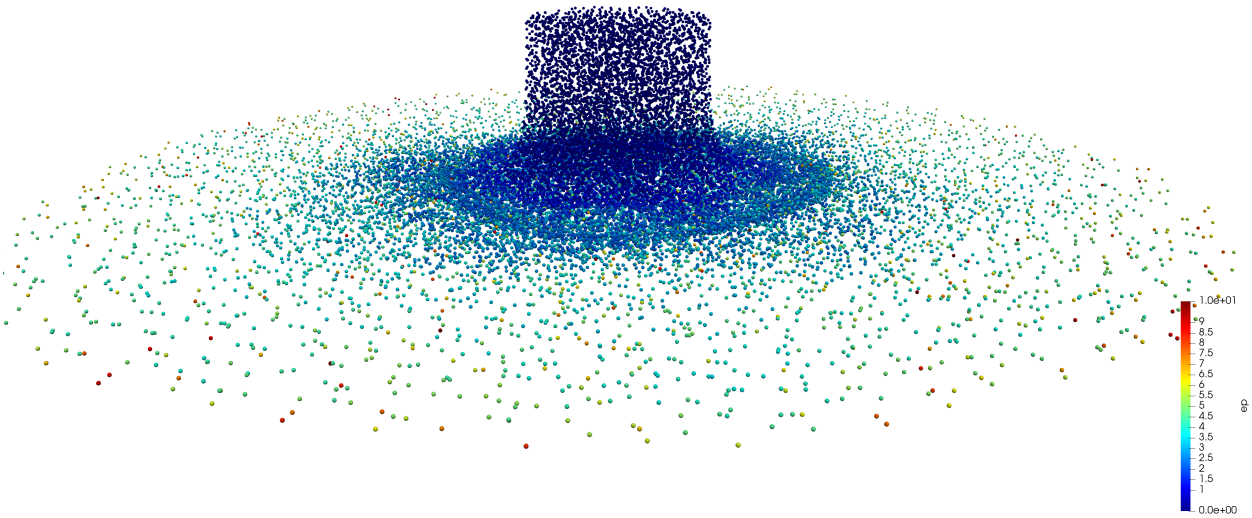

Figure 5-1. Deformed configuration of the Taylor bar at 37μs. The color countour shows the equivalent plastic strain ε_p. The impact velocity has been increased from 227m/s to 750m/s to obtain very large deformation. Note the spread of the points as the cylinder flattens against the rigid surface. This is undesirable for fine resolution of the fields, and thus the need for adaptivity.

5.1. OTM Point and Node Injection

As as starting step, we propose a node and point injection procedure for the OTM method. We introduce new nodes and points as the simulation proceeds where needed as determined by a simple

separation criterion. The existing nodes and points remain, and therefore, no mapping of internal state variables is necessary. Nevertheless, it is necessary to interpolate internal state variables to new material points. To this end, we employ Lie group interpolation and variational recovery to ensure they stay in their proper manifolds [25]. Our initial focus is on capability demonstration, and thus we set a very simple adaptivity metric as shown in Figure 5-2 and Algorithm 2, where a is a specific node, h_a is the distance between that node and its nearest neighbor, and tol is a predefined tolerance. An identical metric and algorithm is used for the points.

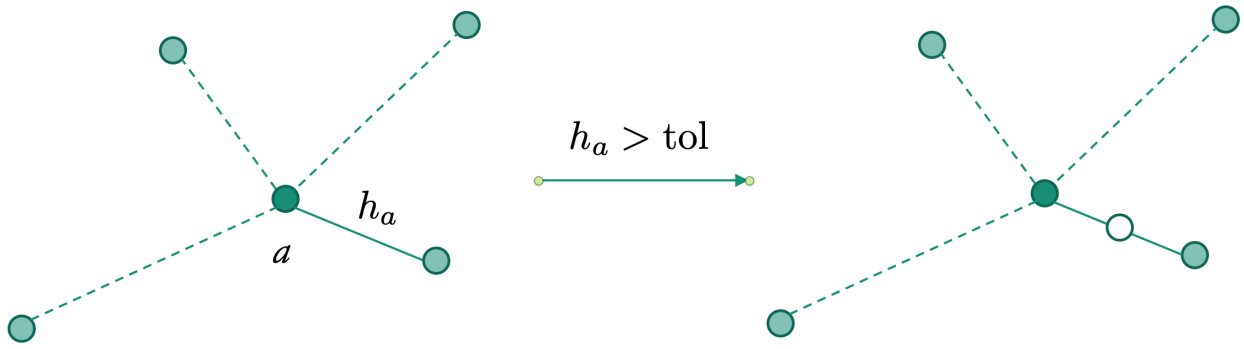

Figure 5-2. Simple distance adaptivity metric, where a is a specific node, h_a is the distance between that node and its nearest neighbor, and tol is a predefined tolerance. An identical metric and algorithm is used for the points.

```
for a ∈ nodes do
    h_a ← min_{b≠a} |x_a − x_b|
    if h_a > tol then
        insert node halfway between
        interpolate fields to new node
    end if
end for
```

Algorithm 2 Simple distance adaptivity metric for nodes. An identical algorithm is used for the points.

As a demonstration of the adaptivity scheme, and in order to be able to visualize the injection of points and nodes, we use an extremely coarse density of nodes and points on the Taylor bar exemplar. The result is shown in Figure 5-3, where we capture two time frames in the simulation before and after an adaptivity step is performed according to Algorithm 2.

5.2. Conditioning of the Point and Node Injection Procedure

Our first attempt to introduce adaptivity to the OTM method uses the simple adaptivity metric described in the previous section. As is evident from Figure 5-2 and Algorithm 2, the newly injected nodes and points are positioned exactly in between existing ones. In our simulations, we notice that this leads to numerical difficulties in the selected Newton solver for the computation of

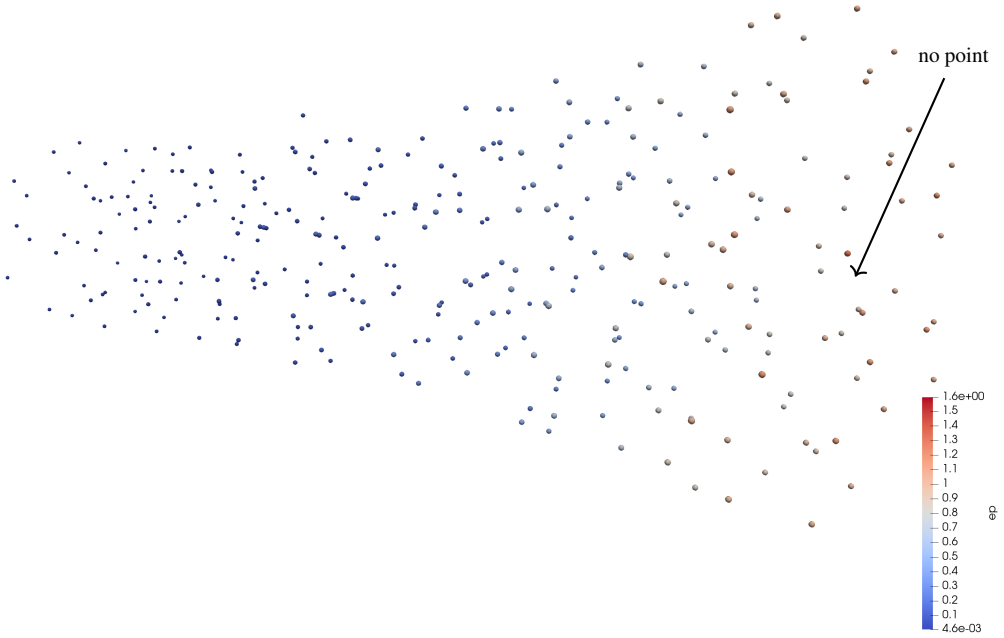

(a) Pre point injection

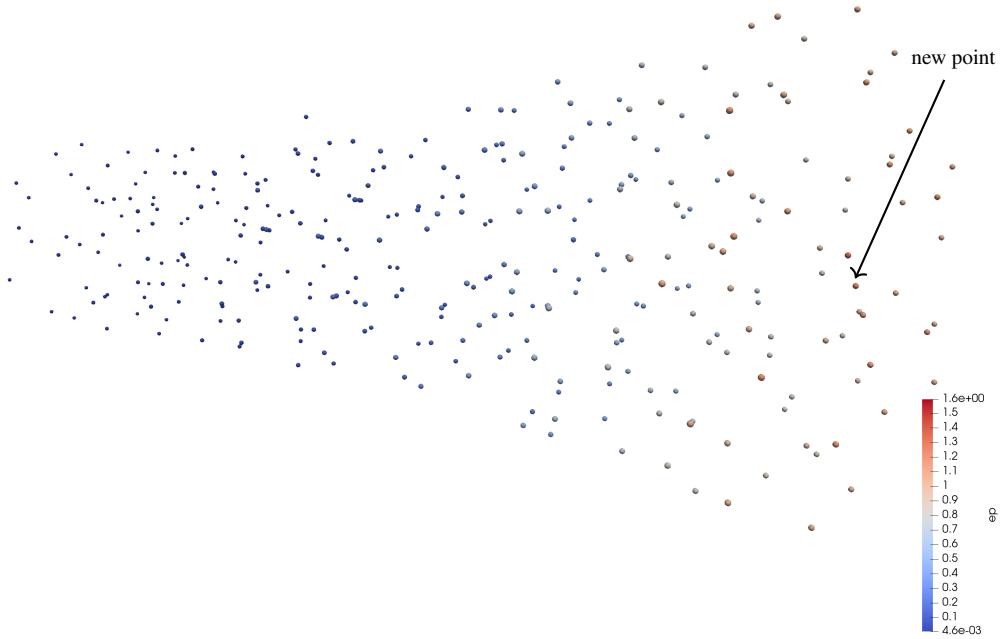

(b) Post point injection

Figure 5-3. Demonstration of the adaptivity procedure of Algorithm 2 on the Taylor bar with an extremely coarse density of nodes and points. Two time frames that capture an instance of point injection. Note the new point near the right end on the bottom figure. There may be other newly injected points.

the LME shape functions. To further investigate this phenomenon, we examine the ability of the Newton solver to compute the LME shape functions by defining a set of nodes and then simulating the injection of a new node anywhere in the cube defined by the set of existing nodes, as shown in Figure 5-4.

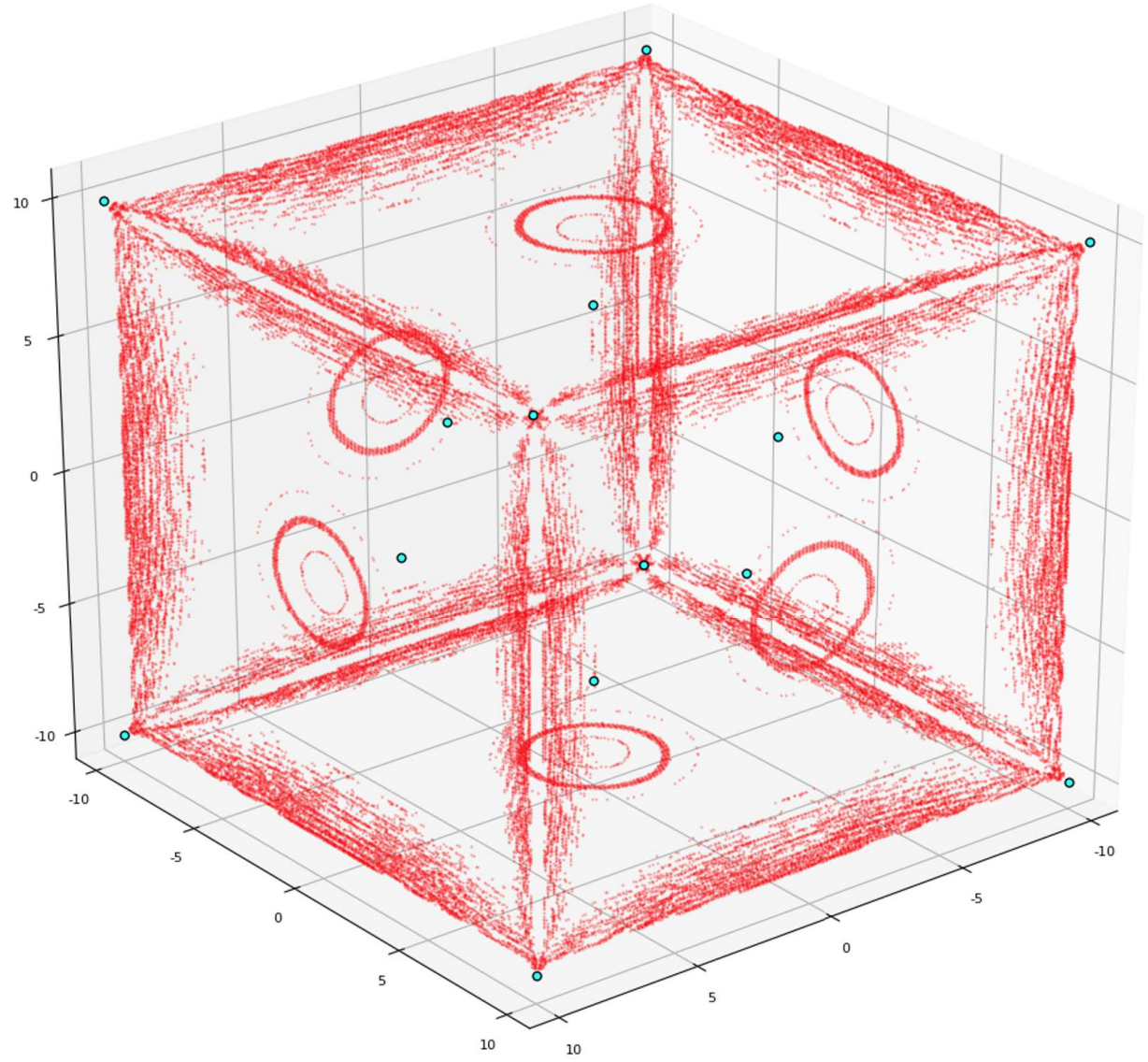

Figure 5-4. Cube domain with a distribution of nodes (light blue) to demonstrate the regions of ill conditioning for the evaluation of the LME shape functions. The red regions indicate where the Newton solver cannot converge to a solution of the LME optimization problem defined in (2.12).

Given this situation, we consider several strategies to overcome this numerical difficulty, such as carefully regulate node and point locations, spatially and temporally adjusting the LME support parameter β defined in (2.12), use rank-deficient linear solvers when the system is singular or combine nonlinear optimization methods. Of all of these, regulating the position of nodes and points would introduce unacceptable restrictions to the OTM method. We consider the remaining

options, and our findings are summarized in Figure 5-5, where we show the success rate of different solvers for the solution of the LME optimization problem (2.12) for the red regions of Figure 5-4.

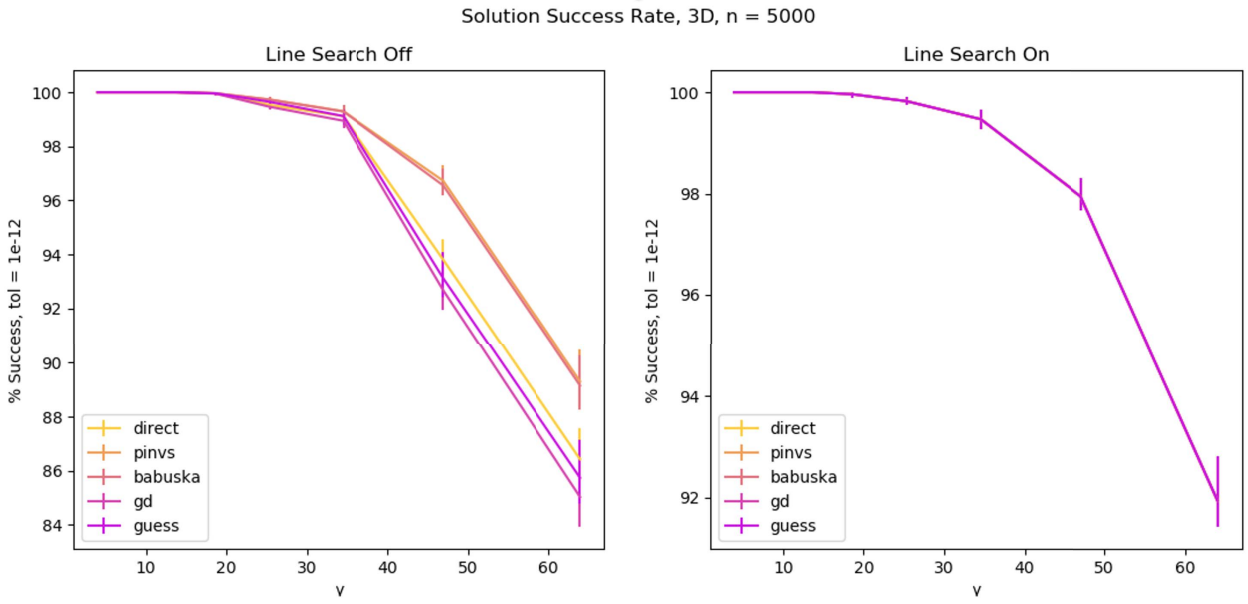

Figure 5-5. Success rate of different solvers for the solution of the LME optimization problem (2.12) for the red regions of Figure 5-4. The parameter γ is related to the parameter β by $\gamma := \beta h^2$, where h is a characteristic distance, often the minimum distance between nearest points. On the left we show the performance of the solvers with no line search. On the right, we use a backtracking line search. Note that the introduction of the line search removes all significant differences between solvers.

It is evident that no matter the solution scheme, introducing a backtracking line search removes all significant differences between solvers. Furthermore, we note that the success rate of the solvers decreases dramatically as γ, and therefore β, increases. The implication is that for ill-conditioned regions, the locality of the LME functions is compromised, and the solvers will only be able to compute shape functions with very wide support. This is undesirable for at least two reasons: it increases significantly the computational cost of the simulations, and introduces a much higher degree of nonlocality into the simulated physical phenomena. For these reasons, we conclude that, although we believe that the node and point injection procedure is sound, introducing new nodes and points in a linear fashion is detrimental to the method. Therefore, we propose to develop more complex and sophisticated injection schemes in future work.

6. CONCLUSION

We leveraged the theory of the Optimal Transportation Meshfree method for extreme deformation. We created an implementation of the method in the open-source LGR framework that may be used for further research and exploration of meshfree methods, adaptivity and extreme deformation. We introduced adaptivity to meshfree simulations, and we leveraged the LGR code for scalability and execution on the GPU. Our team achieved the objectives that we defined for this LDRD project.

In addition, we achieved synergy between 1400, 1500, and 8300 with a strong, extremely capable team. We demonstrated that the OTM method can achieve regimes of extreme deformation naturally and that we can introduce adaptivity to our implementation with relative ease. We also discovered that due to the ill-conditioning of the LME problem, different adativity schemes than the one we proposed are needed, but those are within the scope of future work.

Some of the old habits acquired by many years of use of the finite element are hard to break (no mesh, no elements). Furthermore, some things that are difficult in FEM are relatively easy in OTM and vice versa. We need to develop new intuition through experience. We also learned that we need to develop better adaptivity metrics (variational, energy based), and possibly adopt the use of different shape functions and adaptivity at extreme deformation. Also, we encountered the issue of locking in isochoric deformation, and thus we need to collaborate with staff that are already working on this problem, like Mike Tupek and Jake Koester.

The future promise of OTM is that we may be able to formulate novel, meshfree adaptivity metrics, and access regimes currently inaccessible with existing FEM technology, such as impact on hard and soft targets, simulation of subtractive and additive manufacturing, and phase changes and melting.

BIBLIOGRAPHY

[1] Miquel Aguirre et al. “A vertex centred Finite Volume Jameson-Schmidt-Turkel (JST) algorithm for a mixed conservation formulation in solid dynamics”. In: *JOURNAL OF COMPUTATIONAL PHYSICS* 259 (Feb. 2014), 672–699. ISSN: 0021-9991.

[2] M Arroyo and M Ortiz. “Local maximum-entropy approximation schemes: a seamless bridge between finite elements and meshfree methods”. English. In: *INTERNATIONAL JOURNAL FOR NUMERICAL METHODS IN ENGINEERING* 65.13 (Mar. 2006), 2167–2202. ISSN: 0029-5981.

[3] P. Aubertin, J. Réthoré, and R. de Borst. “Energy conservation of atomistic/continuum coupling”. In: *International Journal for Numerical Methods in Engineering* 78.11 (2009), pp. 1365–1386. ISSN: 1097-0207.

[4] M. E. Backman and S.A. Finnegan. “The propagation of adiabatic shear”. In: *Metallurgical Effects of High Strain Rates* 16 (1973), pp. 531–543.

[5] R.I. Borja. “A finite element model for strain localization analysis of strongly discontinuous fields based on standard Galerkin approximation”. In: *Computer Methods in Applied Mechanics and Engineering* 190.11-12 (2000), pp. 1529 –1549.

[6] R.I. Borja. “Finite element simulation of strain localization with large deformation: capturing strong discontinuity using a Petrov-Galerkin multiscale formulation”. In: *Computer Methods in Applied Mechanics and Engineering* 191.27-28 (2002), pp. 2949 –2978.

[7] J.H. Brunton et al. “The deformation of metals by high velocity impact”. In: *Metals For The Space Age, Plansee Proceedings 1964* (1965), pp. 137–148.

[8] B. Cambou. *Behavior of granular materials*. Springer-Verlag, Vienna, 2014.

[9] F. Feyel. “A multilevel finite element method (FE2) to describe the response of highly non-linear structures using generalized continua”. In: *Computer Methods in Applied Mechanics and Engineering* 192.28-30 (2003). Multiscale Computational Mechanics for Materials and Structures, pp. 3233 –3244. ISSN: 0045-7825.

[10] N.A. Fleck and J.W. Hutchinson. “A reformulation of strain gradient plasticity”. In: *Journal of the Mechanics and Physics of Solids* 49.10 (2001), pp. 2245 –2271. ISSN: 0022-5096.

[11] J.W. Foulk et al. “Extending a 10-Node Composite Tetrahedral Finite Element for Solid Mechanics”. In: *Internaltional Journal of Numerical Methods in Engineering* in press (2020).

[12] P.R. Guduru, A.J. Rosakis, and G. Ravichandran. “Dynamic shear bands: an investigation using high speed optical and infrared diagnostics”. In: *Mechanics of Materials* 33 (2001), pp. 371–402.

[13] E. Gürses. “Aspects of Energy minimization in solid mechanics: evolution of inelastic microstructures and crack propagation”. PhD thesis. Stuttgart, Germany: Institut für Mechanik (Banwesen), Lehrstuhl I, 2007.

[14] M. Heroux et al. *An Overview of Trilinos*. Tech. rep. SAND2003-2927. Sandia National Laboratories Report, Aug. 2003.

[15] Daniel Ibañez. *Lagrangian Grid Reconnection Toolkit*. 2016.

[16] Sandia National Laboratories. *Cubit*. `https://cubit.sandia.gov`. Feb. 2016.

[17] B. Li. “The Optimal Transportation Method in Solid Mechanics”. PhD thesis. California Institute of Technology, 2009.

[18] B. Li, M. Stalzer, and M. Ortiz. “A massively parallel implementation of the Optimal Transportation Meshfree method for explicit solid dynamics”. English. In: *INTERNATIONAL JOURNAL FOR NUMERICAL METHODS IN ENGINEERING* 100.1 (Oct. 2014), 40–61. ISSN: 0029-5981.

[19] B. Li et al. “Large scale Optimal Transportation Meshfree (OTM) Simulations of Hypervelocity Impact”. English. In: *PROCEEDINGS OF THE 12TH HYPERVELOCITY IMPACT SYMPOSIUM*. Ed. by Sorensen, B and Chhabildas, L. Vol. 58. Procedia Engineering. 12th Hypervelocity Impact Symposium (HVIS), Baltimore, MD, SEP 16-20, 2012. SARA BURGERHARTSTRAAT 25, PO BOX 211, 1000 AE AMSTERDAM, NETHERLANDS: ELSEVIER SCIENCE BV, 2013, 320–327.

[20] B. Li, A. Pandolfi, and M. Ortiz. “Material-point erosion simulation of dynamic fragmentation of metals”. English. In: *MECHANICS OF MATERIALS* 80.B, SI (Jan. 2015), 288–297. ISSN: 0167-6636.

[21] B. Li, F. Habbal, and M. Ortiz. “Optimal transportation meshfree approximation schemes for fluid and plastic flows”. English. In: *INTERNATIONAL JOURNAL FOR NUMERICAL METHODS IN ENGINEERING* 83.12 (Sept. 2010), 1541–1579. ISSN: 0029-5981.

[22] B. Li et al. “Verification and validation of the Optimal Transportation Meshfree (OTM) simulation of terminal ballistics”. English. In: *INTERNATIONAL JOURNAL OF IMPACT ENGINEERING* 42 (Apr. 2012), 25–36. ISSN: 0734-743X.

[23] Bo Li. personal communication. Feb. 2020.

[24] J.E. Marsden and Ratiu T.S. *Introduction to Mechanics and Symmetry: A Basic Exposition of Classical Mechanical Systems*. Springer-Verlag, New York, 1999.

[25] Alejandro Mota et al. “Lie-group interpolation and variational recovery for internal variables”. In: *COMPUTATIONAL MECHANICS* 52.6 (Dec. 2013), 1281–1299.

[26] N.M. Newmark. “A method of computation for structural dynamics”. In: *Journal of Engineering Mechanics, ASCE* 85.3 (1959), pp. 67–94.

[27] J. Nocedal and S.J. Wright. *Numerical Optimization*. New York: Springer, 1999.

[28] M. Ortiz and L. Stainier. “The variational formulation of viscoplastic constitutive updates”. In: *Computer Methods in Applied Mechanics and Engineering* 171.3-4 (1999), pp. 419–444.

[29] J. T. Ostien et al. “A 10-node composite tetrahedral finite element for solid mechanics”. In: *International Journal for Numerical Methods in Engineering* (2016). doi:10.1002/nme.5218, n/a–n/a. ISSN: 1097-0207.

[30] H. C. Rogers. “Adiabatic plastic deformation”. In: *Annual Review of Materials Science* 9 (1979), pp. 283–311.

[31] G.I. Taylor. “The use of flat-ended projectiles for determining dynamic yield stress I. Theoretical considerations.” In: *Proceedings of the Royal Society A* 194 (1948), pp. 289–299.

[32] H. Tresca. “On further application of the flow of solids”. In: *Proceedings of the Institution of Mechanical Engineerings* 30 (1878), pp. 301–345.

[33] C. Weissenfels and P. Wriggers. “Stabilization algorithm for the optimal transportation meshfree approximation scheme”. English. In: *COMPUTER METHODS IN APPLIED MECHANICS AND ENGINEERING* 329 (Feb. 2018), 421–443. ISSN: 0045-7825.

[34] A.C. Whiffin. “The use of flat-ended projectiles for determining dynamic yield stress II. Tests on various metallic materials.” In: *Proceedings of the Royal Society A* 194 (1948), pp. 300–322.

[35] M.L. Wilkins and M.W. Guinan. “Impact of cylinders on a rigid body.” In: *Journal of Applied Physics* 44.3 (1973), pp. 1200–1206.

[36] Q. Yang, A. Mota, and M. Ortiz. “A class of variational strain-localization finite elements”. In: *International Journal for Numerical Methods in Engineering* 62.8 (2005), pp. 1013–1037. ISSN: 1097-0207.

[37] M. Zhou, A.J. Rosakis, and G. Ravichandran. “Dynamically propagating shear bands in impact-loaded prenotched plates .1. Experimental investigations of temperature signatures and propagation speed”. In: *Journal of the Mechanics and Physics of Solids* 44.6 (1996), pp. 981–1006.

Sandia National Laboratories is a multimission laboratory managed and operated by National Technology & Engineering Solutions of Sandia LLC, a wholly owned subsidiary of Honeywell International Inc., for the U.S. Department of Energy's National Nuclear Security Administration under contract DE-NA0003525.